Hindawi
Geofluids
Volume 2024, Article ID 6642676, 18 pages
https://doi.org/10.1155/2024/6642676

Research Article

Experimental and Numerical Simulation Study of Water Infiltration Impact on Soil-Pile Interaction in Expansive Soil

Waleed Awadalseed,[1] Xingli Zhang,[1] Yunpeng Ji,[1] XiangJin Wang,[2] Yuntian Bai,[1] and Honghua Zhao[3]

[1]*State Laboratory of Structural Analysis for Industrial Equipment, Department of Engineering Mechanics, Dalian University of Technology, China 116023*
[2]*DUT-BSU Joint Institute, Dalian University of Technology, China*
[3]*State Key Laboratory of Structural Analysis for Industrial Equipment, Department of Engineering Mechanics, International Research Center for Computational Mechanics, Dalian University of Technology, China 116023*

Correspondence should be addressed to Honghua Zhao; zhaoh@dlut.edu.cn

Received 2 June 2023; Revised 14 November 2023; Accepted 11 December 2023; Published 17 January 2024

Academic Editor: Qingchao Li

A laboratory model of a single pile embedded in Nanyang expansive soil and subjected to water infiltration is applied in this study to examine the interaction between the expansive soil and pile foundation upon water infiltration. The soil matric suction decreases as a result of the rising soil-water content. The amount of soil ground heave reaches its peak of 10.7 mm after 200 hours of water infiltration. As matric suction decreases, pile shaft friction also declines, which causes more of the load at the pile head to be carried by the pile base resulting in more pile settlements. A new numerical simulation method is provided to simulate this issue by coupling the subsurface flow, soil deformation, and hygroscopic swelling to investigate the expansive soil-pile response upon water infiltration. From the numerical simulation model, hygroscopic strain arises as a result of elevated moisture levels resulting from the entry of water, and due to ground heave and the mobilization of lateral soil swelling, the shear stress at the interface between the soil and the pile gradually increases over time. It reaches its maximum value of 4420 Pa at upper depths around 200 hours after the infiltration. The comparison between the lab model testing data and the numerical model results demonstrates a good level of concurrence.

1. Introduction

Water infiltration may lead to altering the moisture levels in the soil. In the case of expansive soils, these changes in moisture content mostly occur due to seasonal fluctuations. As a consequence, the expansive soil experiences either settlement or ground heave due to wetting and drying [1–4], and as a result of increased moisture content induced by water infiltration, the shear strength of unsaturated soil begins to decrease as the negative pore water pressure increases, which is one of the cause of slope instability [5–7]. The investigation of the impact of moisture content fluctuations caused by infiltration on the mechanical properties of unsaturated soil and its implications for the stability of structural foundations has become a prominent area of interest in civil and geomechanical research [8–16]. The investigation of soil-pile interaction is a crucial field of study when examining the interaction between soil and structures [17–20]. Water infiltration triggered changes in the water content of the surrounding soil, which impacted the soil-pile interface strength and load transfer mechanisms. As a result of these alterations in the depth affected by water infiltration, upward friction arises along the pile as a result of displacement between the pile and surrounding soil [21]. The intensity of upward force is determined by increasing lateral earth pressure, taking into account the lateral swelling pressure and water content-dependent interface strength. As a consequence, once the pile moves upward, negative friction develops in the stable zone (the depth not influenced by water infiltration), reducing the pile's bearing capacity

considerably [22–24]. Hence, it could be concluded that the main variables that influence soil-pile interaction during infiltration are net normal stress, matric suction, and interface shear strength characteristics. The challenges associated with the investigation of soil-pile interaction arise from the utilization of either field testing or analytical analysis methodologies in conducting these investigations. On the other hand, analytical analysis involves complex constitutive relationships that encompass several soil factors, whereas field pile testing is typically associated with significant expenses and time constraints. As a result, the studies undertaken on the impact of water infiltration on the interaction between expansive soil and pile foundations have been relatively few. Prior studies have examined the utilization of numerical simulation to investigate the interaction between soils and piles [25–27]. Nevertheless, there is a lack of investigations that have examined the simulation of the interaction between expansive soil and piles, specifically in terms of deformation arising from soil swelling caused by water infiltration.

In this study, a laboratory experiment was done utilizing a simplified methodology and equipment, employing a laboratory-scale model of a single pile embedded in expansive soil subjected to water infiltration. The model is utilized to evaluate the temporal variations in soil moisture levels at various depths inside the soil during the course of infiltration, soil and pile displacement, axial force distribution within the pile, and pile base resistance. Secondly, this study presents a new numerical simulation methodology that integrates the interplay of subsurface flow, soil deformation, and hygroscopic swelling principles. The objective is to examine the interaction between piles and expansive soil in the context of water infiltration. Furthermore, the laboratory test model is employed to verify the results of the proposed numerical simulation methodology. The present work is aimed at introducing a new numerical simulation model and a laboratory model with the objective of enhancing comprehension of the expansive soil-pile interaction during water infiltration.

2. Experimental Model

2.1. Nanyang Expansive Soil. The expansive soil used for this study was imported from Nanyang, Henan Province, China. The soil has been air dried, sealed in plastic bags, and maintained in a humidity-controlled environment. The essential geotechnical properties of the Nanyang soil are determined using the Atterberg limits tests, specific gravity tests, Proctor soil compaction tests, filter paper methods, and constant head permeability tests. The measured findings indicate that soil specimen swelling occurred at a moderate rate. The basic characteristics of Nanyang's expansive soil are shown in Table 1.

The soil-water characteristic curve (SWCC) of the soil sample was determined using the filter paper method. The filter paper process outlined in the ASTM D5298 standard was utilized to carry out the experiment. The obtained data for the soil-water characteristic curve (SWCC) was then analyzed using Van Genuchten's model. This analysis is aimed at determining the saturated and residual volumetric water contents of the soil specimens [28]. The primary aim of conducting the filter paper method is to evaluate the variability of soil matric suction when water infiltrates the soil. This is achieved by applying the soil-water characteristic curve (SWCC) to retrospectively compute the corresponding volumetric water content and matric suction.

Table 1: The physical mechanic parameters of Nanyang's expansive soil.

Properties	Value
Liquid limit (%)	49
Plastic limit (%)	25
Plasticity index	25
Specific gravity	2.61
Maximum dry density (g/cm^3)	1.55
Optimum moisture content (%)	25.5
Saturated volumetric water content, θ_s (%)	41
Residual volumetric water content, θ_r (%)	9
Permeability, k (m·s^{-1})	1.43×10^{-7}
Free swelling index (%)	82%

2.2. Infiltration Test of Soil-Pile Model. The test tank was a cylindrical PVC tank with an internal diameter of 300 mm and a height of 700 mm. An aluminum tube measuring 600 mm in length and 20 mm in diameter was used as a pile model to demonstrate the processes necessary to set up the pile for the test. Figure 1 displays the model pile set up. Strain gauges were placed along the pile surface at different depths (12 cm, 24 cm, 36 cm, and 48 cm) to measure axial strain. In order to keep water from damaging the gauges, they were sealed off, and isolation tape was used to protect the gauges. A 3 mm coating of sand and cement was placed onto the pile surface. This coating layer is to make a surface similar to the prepared rough surface in the interface direct shear test, which was detailed earlier. A steel tank 20 cm in height and 15 cm in diameter is used for the load tank, and load plates totaling 300 N are placed in the load tank. A pressure cell is used to record the load at the pile base, and two computer devices are used to read the data from strain gauges and pressure cells. The infiltration test objectives defined the test tank and model pile dimensions. It was recognized that a larger soil model would present challenges in a laboratory setting, while a smaller model would not accurately capture the representative pattern of soil-pile interaction upon water infiltration, such as the variation of soil-water content and soil matric suction that emulates actual conditions and the distribution of pile axial force along the pile shaft. The test tank accommodated compacted expansive soil layers. A space for the expected ground heave and sand layer beneath the pile was considered. Thus, the pile was designed to sink a 50 cm section of the pile shaft into the soil. There leaves a 10 cm portion space above the soil surface. The tests conducted on the soil utilized in this study have revealed a moderate swelling characteristic. It has been determined that the PVC tank is an appropriate choice for

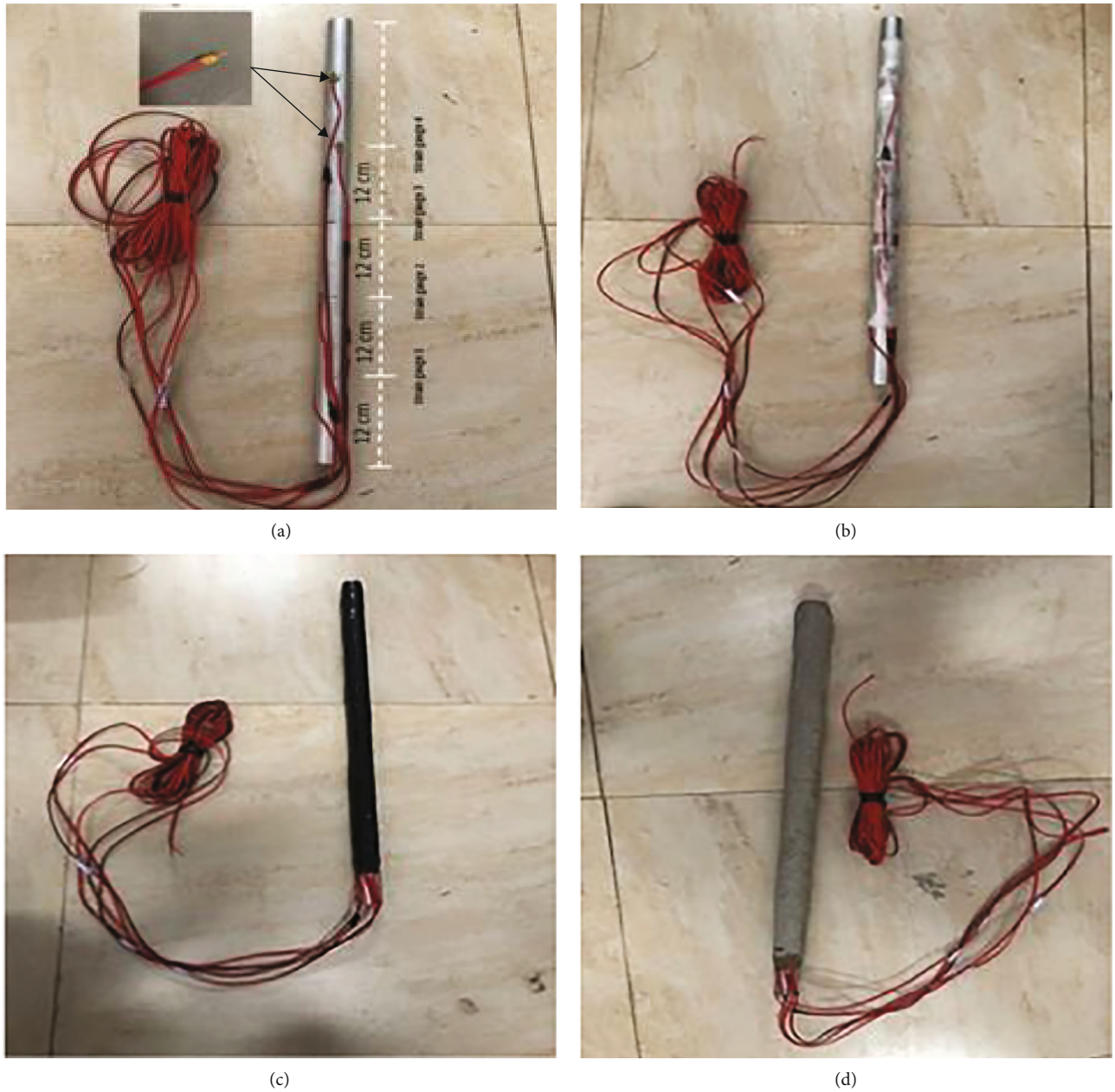

Figure 1: Preparation of the model pile: (a) strain gauge installation, (b) gauge isolation, (c) pile surface isolation, and (d) applied sand-cement layer.

effectively confining the horizontal swelling of the soil within acceptable boundaries.

The embedded pile in the expansive soil is comparable to the idea of floating piles that Nelson et al. (2012) introduced and that Liu and Vanapalli further explored [29, 30]. Consequently, the distribution of axial force in the pile, the heave of the soil, and the displacement of the pile will be recorded.

The experimental settings during the pile infiltration test are shown in Figure 2. The interior of the PVC test tank's wall was taped with a waterproof ruler. The test tank is filled to a height of 100 mm with fine sand at the bottom to be the pile base. To keep the model pile in place during the compaction process, a bolt was used to hold it to the loading machine. A load cell was mounted on the sand layer at the pile model's base, as shown in Figure 2(b), to record the pile base resistance. After these preliminary procedures, the soil was compacted into several layers with an initial water content of 21%, as shown in Figure 2(a), to achieve a wet density of 1.82 g/cm^3 (i.e., a dry density of 1.5 g/cm^3). Three water content sensors (i.e., Soil Moisture Sensor RS485 produced by Sichuan Weinasa Technology Co., Ltd.) are used to measure the variation of water content through the soil body, as indicated in Figure 2(c), and were inserted at various points of Nanyang soil (i.e., top, middle, and bottom) during the compaction, and the load cell cable was connected to a computer to collect the data. The plastic wrap was also applied

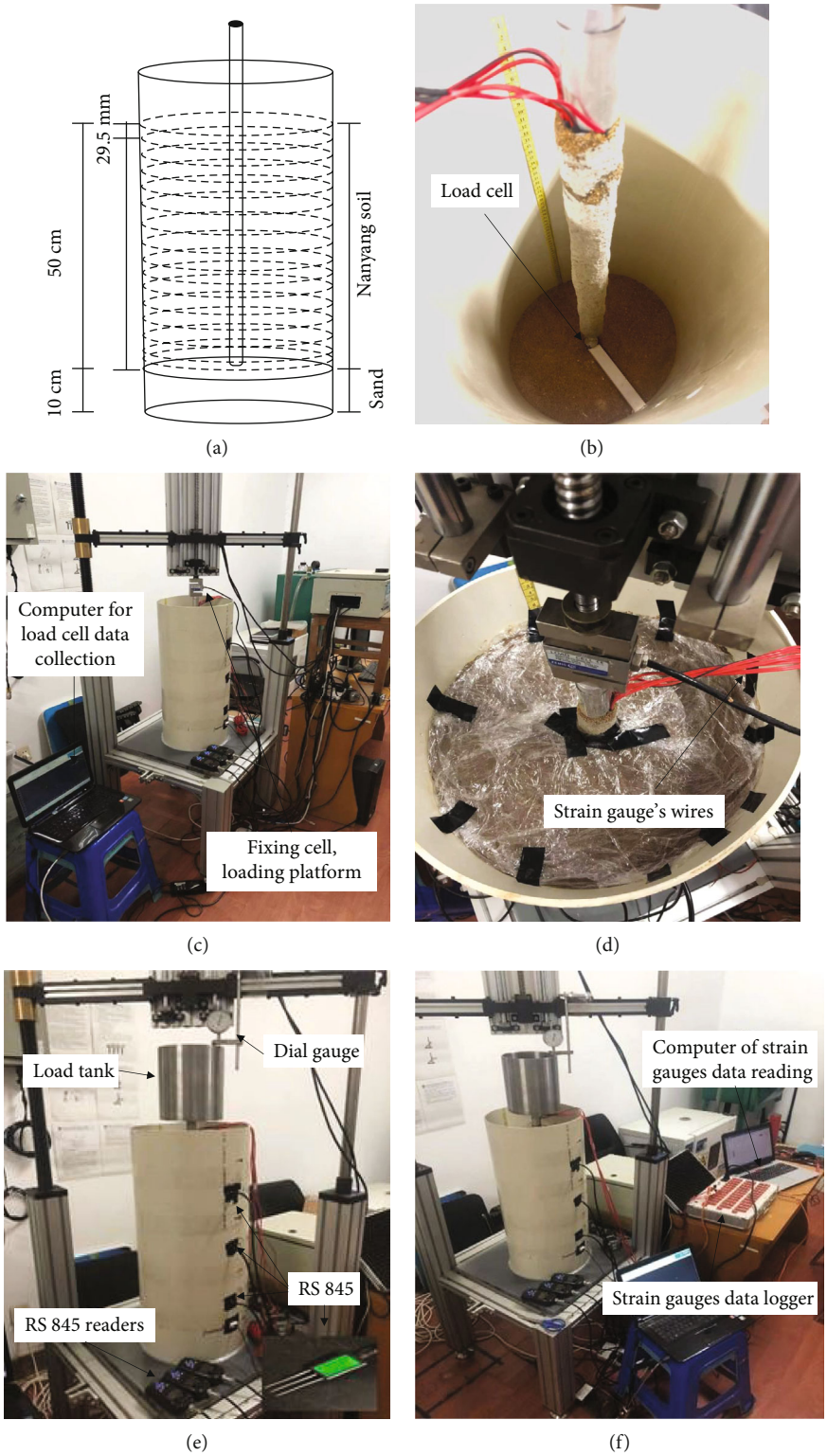

Figure 2: Pile infiltration test model.

over the compacted soil surface to prevent evaporation losses (see Figure 2(d)). The load tank was then set on top of the pile head after the fixing cell that had held the pile in place was removed. 300 N of pile head load was applied to the pile head using load plates. A dial gauge was placed on top of the load tank, as shown in Figure 2(e), to monitor pile settlement throughout the loading and infiltrating phases. Upon noticing that the pile head's displacement had remained stable for one day, the infiltration phase commenced 120 hours after the initiation of the test, during

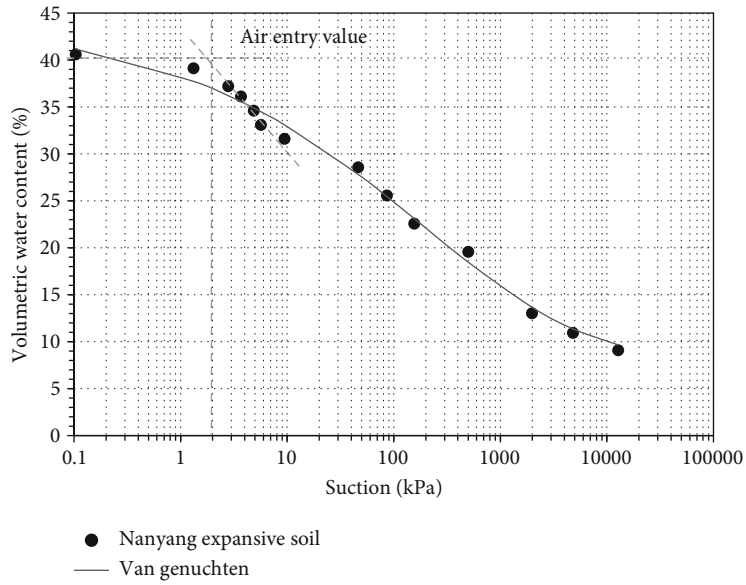

Figure 3: SWCC of Nanyang expansive soil.

which water was manually poured as necessary to sustain a ponding water layer on the soil surface (approximately, 0.05 m). The aforementioned procedures were carried out until the soil achieved full saturation, as determined by soil moisture sensors and visually visible on the muddy soil surface.

3. Result and Discussion

3.1. Soil-Water Characteristic Curve (SWCC). The SWCC of expansive soil specimens is depicted in Figure 3. The obtained saturated volumetric water content (θ_s) was 41%, while the residual volumetric water content (θ_r) of expansive soil where no water is drained was nearly at 9%. The experimental data demonstrate good agreement with the Van Genuchten's [28] model to estimate soil-water retention curves, which were stated in terms of the following equation:

$$\theta = \frac{\theta_s}{\left[1 + (\alpha h)^n\right]^{1-1/n}}, \tag{1}$$

where θ is the volumetric water content of soil ($cm^3\,cm^{-3}$), h is the matric suction (kPa), θ_s is the soil saturated water content, and α and n are the parameters of the model. Utilizing a nonlinear least squares approach, Eq. (1) was adapted to the measured values of each soil specimen with a good fitting.

3.2. Infiltration Test of Soil-Pile Model. Figure 4 illustrates the displacement of both the soil and pile over the duration of the test. The infiltration processes exhibited notable vertical displacement, revealing the occurrence of ground heave. The test tank's walls restrict the lateral expansion of the soil, which is the cause of this phenomenon. Following the initial 24-hour period of infiltration, the occurrence of ground heave is initially minimal and gradually becomes more noticeable. Following a period of 350 hours of infiltration, the soil underwent a process resulting in the generation of a ground heave measuring 10.7 mm. The settling of the pile head exhibited an initial magnitude of approximately 0.6 mm during the static loading phase, which subsequently increased to roughly 4 mm at the end of the test. A potential correlation may be observed between a reduction in pile shaft friction and a decline in matric suction, which may have led to an increase in the load borne by the pile toe and subsequently resulted in more pile displacement. In comparison to the results reported in Liu and Vanapalli's model [21], the soil and the pile displacement in this study exhibit a similar trend. However, the magnitudes of soil ground heave and pile displacement are noticeably smaller. This discrepancy can be attributed to two factors. Firstly, the soil utilized in this model possesses lower swelling properties compared to the soil employed in Liu and Vanapalli's model. Secondly, the load applied to the pile head in this study is small.

Figure 5 illustrates the volumetric measurement of water content in the sample, whereas Figure 6 displays the observed variations in suction levels during the testing process. Based on the observations depicted in Figure 5, it is evident that the upper layer of soil took approximately 50 hours to undergo complete permeation by water during the commencement of the infiltration process. As the soil depth grew, there was a modest increase in the duration required for full saturation. In ultimately, it was observed that all soil layers, with a uniform depth of 430 mm, achieved a state of full saturation. The reason for the delay in attaining complete saturation in the lower layer can be ascribed to the migration of the wetting front from the soil surface to the soil bottom, considering the permeability of the soil. It is conceivable that the lower stratum may necessitate a lengthier duration to attain a state of complete saturation. The observed variations in the saturation condition of the soil sample, as depicted by the abrupt shifts in the curves shown in Figure 5, can be attributed to the significant rise in void ratio resulting from the volume expansion of the expansive

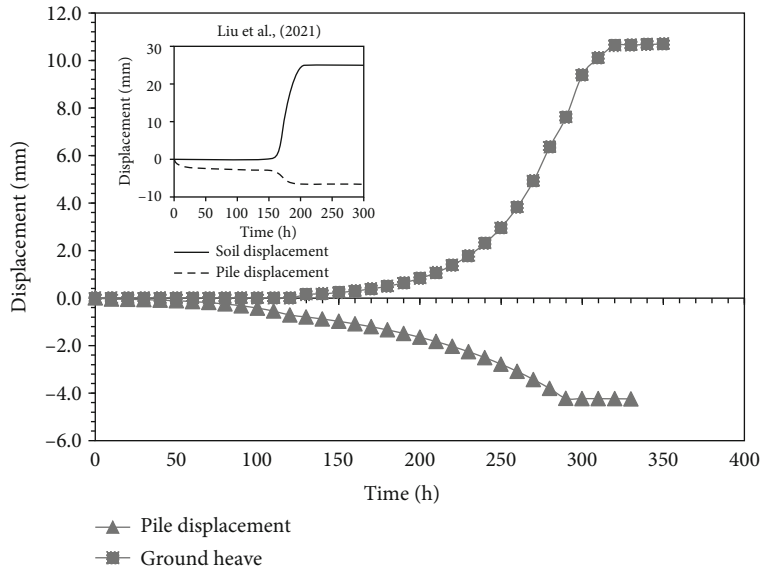

Figure 4: Soil ground heave and pile settlement.

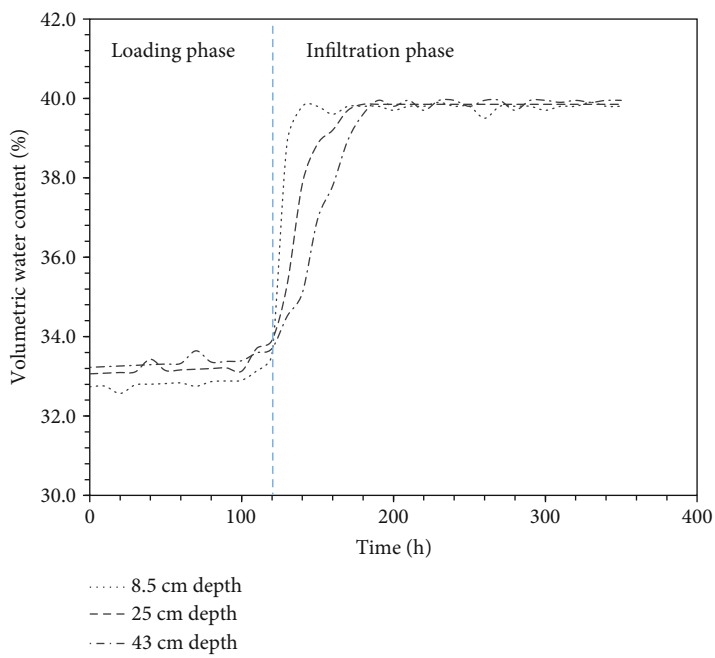

Figure 5: Variations in the distribution of volumetric water content over time.

soil. This phenomenon was achieved due to the implementation of hand irrigation, which effectively retains water at the soil surface, hence expediting the process to a considerable extent. Furthermore, when the volume of the expansive soil increases, there is a corresponding proportional rise in the void ratio. The soil, which was analyzed from the surface of the ground, exhibited degradation into a muddy state subsequent to the execution of an infiltration test. The rate of ground heave advancement is inversely related to the change in volumetric water content, or suction.

The determination of pile axial forces involves the measurement of strains induced in the shaft. This is achieved by employing strain gauges that are affixed at four specific locations along the shaft. The axial force was determined by employing the following equation [31]:

$$P = \varepsilon E_{\mathrm{p}} A_{\mathrm{C}}, \tag{2}$$

where P is the axial force generated in the pile shaft, ε is the recorded strain, E_{p} is the elasticity modulus of the material of the pile, and A_{C} is the cross-sectional area of pile shaft.

Figure 7 depicts a noticeable pattern in which the axial force of the pile progressively increased throughout the different phases of the soil infiltration test. The manifestation

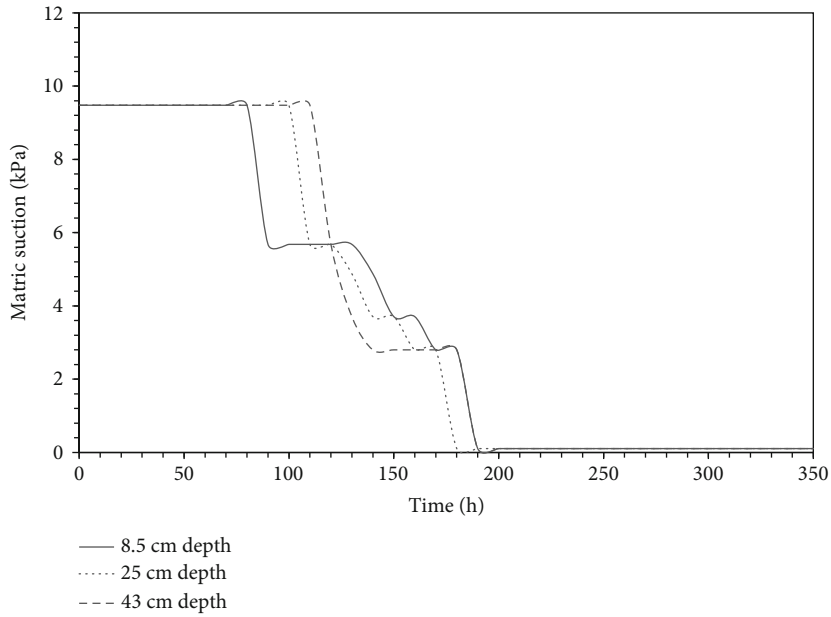

Figure 6: Matric suction variation.

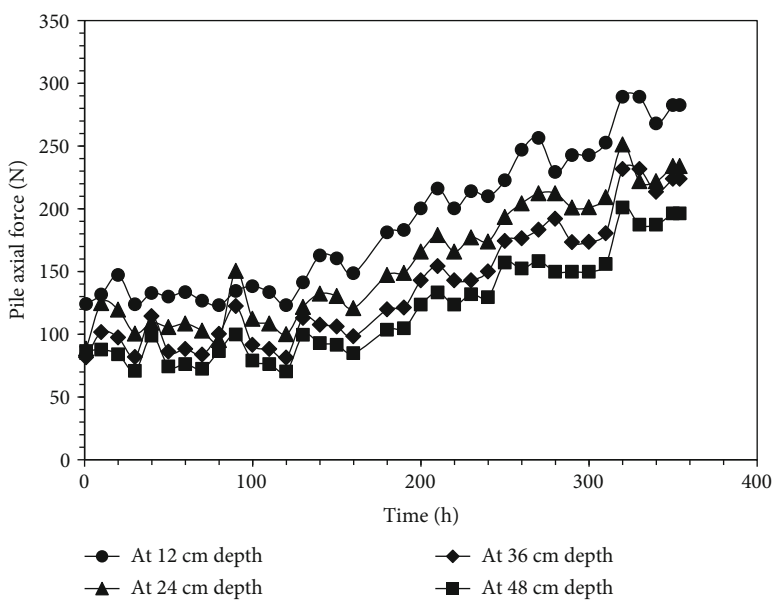

Figure 7: Pile axial force distribution along the pile length.

of axial force in the pile got more pronounced as depth and time increased. The aforementioned occurrence can be explained by the observation that, during the period of static loading, the positive frictional force was evenly distributed down the whole length of the pile. Upon reaching its saturation point, the expansive soil gave rise to the development of negative and positive frictions in the top and lower regions of the pile, respectively. To provide further clarification, it can be observed that the positive shaft friction experienced in the lower portion of the pile, as well as at its base, exhibits a greater capacity to carry more loads. However, the magnitude of the adverse friction in the top region subsequent to infiltration surpasses the beneficial friction observed prior to infiltration. The observed discrepancy may be attributed to the substantial increase in relative displacement between piles and soil caused by ground motion.

Based on the results shown in Figure 8, it can be seen that the progressive loading stages of the pile before infiltration caused a small increase in the resistance of the pile base. Eventually, it reached a stable level of 22 N during the static loading phase. This suggests that the majority of the upper load was mostly supported by the shaft friction, which shows

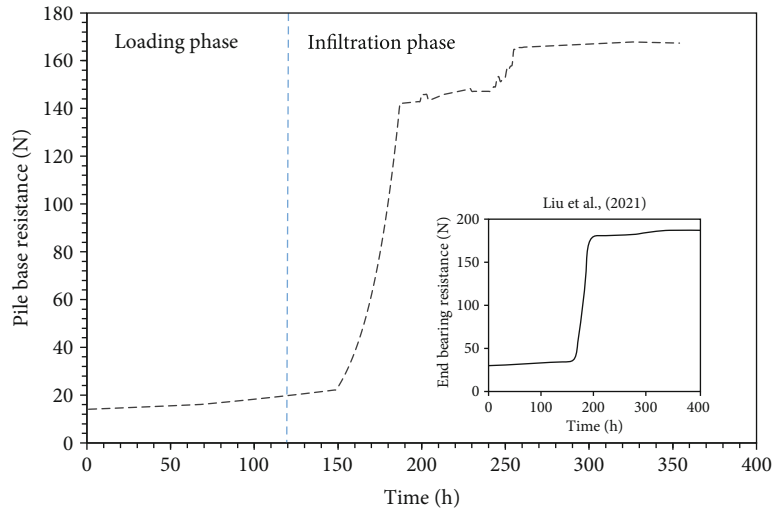

Figure 8: The pile base resistance over time.

that the pile behaved like a floating pile. The infiltration starts at 120 hours. Throughout a span of 60 hours of infiltration, the resistance experienced a subsequent increase, reaching a value of 142 N, and this could be attributed to the decreases in soil suction due to the increase in soil-water content, resulting in a decrease in shaft friction. Ultimately, during a cumulative infiltration time period of about 100 hours, the pile base resistance reached a state of equilibrium, settling at a magnitude of 168 N. The increased resistance measured at the base of the pile indicates a decrease in the friction experienced by the pile shaft during the infiltration process. The occurrence of suction within pile shafts can be attributed to the decrease in friction, resulting in a subsequent augmentation of pile settlements. The observed drop can be attributed to the shift in load distribution from the upper to the lower portion of the pile. The observed phenomenon of soil stress relaxation, characterized by the progressive transformation of elastic deformation into plastic deformation, may potentially explain the marginal yet discernible augmentation in pile base resistance subsequent to the full saturation of the expansive soil. The soil and pile displacement patterns, along with the resistance seen at the pile base, demonstrate resemblances to the experimental model done by Liu and Vanapalli [21]. The attainment of the maximum value of pile base resistance may have been delayed beyond the initial 40-hour period due to the gradual process of complete saturation of the soil at greater depths.

4. Numerical Simulation Model

4.1. Theoretical Principle and Governing Equations. The numerical simulation method is based on the utilization of the governing partial differential equations (PDEs) that describe water flow and soil deformation. The equations are subsequently solved in a linked manner with a finite element method (FEM) solver (COMSOL Multiphysics software). The combination of hydraulic phenomena, namely, the movement of water through porous media (expansive soil), with mechanical phenomena, such as the deformation of soil, is achieved by the use of volume change (hygroscopic strain). Both the porous matrix and the fluid martial characteristics and constitutive equations have been defined. The mechanical and hydraulic boundary conditions are also defined. The hygroscopic swelling feature acts as ground heave which is correlate to soil-pile relative displacement caused by changes in moisture content. A time-dependent and stationary solver was used in the simulation model. To elaborate on the modelling process, more information about the modelling approach used is provided. Specifically, the use of the solid mechanics and Richards' equation interfaces within the COMSOL Multiphysics software to simulate water flow and soil deformation processes.

4.1.1. Richards' Equation. The Richards' equation physics interface studies flow in variably saturated porous media. Hydraulic characteristics alter when fluids travel through the media, filling some pores and emptying others with variably saturated flow. Richards' equation appears to be comparable to Darcy's law's saturated flow equation; however, it is notoriously nonlinear. Nonlinearities occur as the material and hydraulic properties change from unsaturated to saturated. Hence, in this study, the flow in the variably saturated soil domain is evaluated using the Richards' equation as governing equation from the porous media and subsurface flow module which is shown below:

$$\rho\left(\frac{C_{\mathrm{m}}}{\rho g}+s_{\mathrm{e}}s\right)\frac{\partial P}{\partial t}+\nabla\bullet\rho_{\mathrm{f}}(\mathbf{u})=Q_{\mathrm{m}},$$
$$\mathbf{u}=-\frac{k_{\mathrm{s}}}{\mu}k_{\mathrm{r}}(\nabla P+\rho_{\mathrm{f}}g\nabla D), \tag{3}$$

where $\mathbf{u}$ represent the flux vector and the pressure, P, is the dependent variable. In this equation, C_{m} represents the specific moisture capacity which connects changes in soil moisture to inflow rate, S_{e} denotes the effective saturation, S is the

storage coefficient, k_s gives the hydraulic permeability, μ is the fluid dynamic viscosity, k_r denotes the relative permeability, ρ_f is the fluid density, g is acceleration of gravity, D represents the elevation, and Q_m is the fluid source.

Van Genuchten's analytic formulas were available for simulating variably saturated flow, which occurs when fluid properties change as fluids move through the soil domain. The volumetric water content (θ), effective saturation (S_e), specific moisture capacity (C_m), and relative permeability (k_r) were determined by the analytic formulas of Van Genuchten as follows:

$$\begin{aligned}
\theta &= \begin{cases} \theta_r + S_e(\theta_s - \theta_r) & H_P < 0, \\ \theta_s & H_p \geq 0, \end{cases} \\
S_e &= \begin{cases} \dfrac{1}{\left[1 + |\alpha H_P|^n\right]^m} & H_P < 0, \\ 1 & H_p \geq 0, \end{cases} \\
C_m &= \begin{cases} \dfrac{\alpha m}{1-m}(\theta_s - \theta_r) S_e^{1/m}\left(1 - S_e^{1/m}\right)^m & H_P < 0, \\ 0 & H_P \geq 0, \end{cases} \\
k_r &= \begin{cases} (s_e)^\lambda \left[1 - \left(1 - s_e^{1/m}\right)^m\right]^2 & H_P < 0, \\ 1 & H_P \geq 0, \end{cases}
\end{aligned} \tag{4}$$

where H_P is pressure head, n and m are the shape parameters of soil-water characteristic ($m = (1 - (1/n))$), and λ is the model constant and is assumed to be 0.5 in the traditional Van Genuchten model; in COMSOL $\lambda = (2/n) + l + 2$, l is the model parameter that determines the relative permeability.

4.1.2. Hygroscopic Swelling. Hygroscopic swelling is a phenomenon that occurs when materials expand in volume as a result of their inclination to absorb moisture from the environment and therefore storing it. Moisture absorption and storage cause the material to swell, inducing stresses and strains. Although hygroscopic swelling is an essential attribute of expansive soil, it is worth noting that many other materials, such as paper, cotton, wood, nylon, sugar, and a range of other materials, are also hygroscopic. Some studies have examined and modelled the hygroscopic swelling behavior of rice and other materials [32–36]. As the hygroscopic swelling induces deformations on the free boundaries while increasing compression inside the model domain, it is suitable for simulating soil swelling behavior and the subsequent ground heave. This might correspond to the actual scenario of soil ground heave in the laboratory model where the lateral swelling of the soil is limited by the tank wall allowing the swelling to occur vertically.

To assess the soil deformation caused by water adsorption, a series of equations are provided for determining the hygroscopic swelling coefficient within the linear elastic material node utilizing the solid mechanic interface.

The governing equation for the linear elastic material node in solid mechanics is as follows:

$$\rho_a \frac{\partial^2 u}{\partial t^2} = \nabla.(FS)^T + Fv. \tag{5}$$

Equation (5) represents the equation of motion, where u is displacement factor, Fv is the force per deformed volume, F is the deformation gradient tensor, S strain rate tensor, ρ_a is the density, and T is the temperature.

In terms of the displacement gradient, the deformation gradient tensor F can be written as

$$F = I + \nabla u, \tag{6}$$

where I is the unity matrix.

And strain rate tensor can be defined as

$$S = F^{-T} \varepsilon F^{-1}, \tag{7}$$

where ε is the strain tensor that can be defined from the Green-Lagrange strain tensor:

$$\varepsilon = \frac{1}{2}\left(F^T F - I\right). \tag{8}$$

For the hygroscopic swelling, the governing relation of hygroscopic deformation gradient tensor (F_{hs}) and the hygroscopic strain tensor (ε_{hs}) is expressed as follows:

$$F_{hs} = I + \varepsilon_{hs}. \tag{9}$$

The hygroscopic swelling strain can be defined by employing Hooke's law for hygroscopic materials:

$$\{\varepsilon\} = [d]^{-1}\{\sigma\} + \left\{\varepsilon^{\text{hygro}}\right\}, \tag{10}$$

where $\{\sigma\}$ is the stress tensor.

$$\{\sigma\} = \left[\sigma_x\, \sigma_y\, \sigma_z\, \sigma_{xy}\, \sigma_{yz}\, \sigma_{xz}\right]^T. \tag{11}$$

$\{\varepsilon\}$ is the strain vector.

$$\{\varepsilon\} = \left[\varepsilon_x \varepsilon_y\, \varepsilon_z\, \varepsilon_{xy}\, \varepsilon_{yz}\, \varepsilon_{xz}\right]^T. \tag{12}$$

$[d]^{-1}$ is the compliance matrix expressed in terms of Young's modulus (E), shear modulus (G), and Poisson's ratio.

$$[d]^{-1} = \begin{bmatrix} \frac{1}{E} & \frac{-\nu}{E} & \frac{-\nu}{E} & 0 & 0 & 0 \\ \frac{-\nu}{E} & \frac{1}{E} & \frac{-\nu}{E} & 0 & 0 & 0 \\ \frac{-\nu}{E} & \frac{-\nu}{E} & \frac{1}{E} & 0 & 0 & 0 \\ 0 & 0 & 0 & \frac{1}{G} & 0 & 0 \\ 0 & 0 & 0 & 0 & \frac{1}{G} & 0 \\ 0 & 0 & 0 & 0 & 0 & \frac{1}{G} \end{bmatrix}, \quad G = \frac{E}{2(1+\nu)}. \tag{13}$$

$\{\varepsilon^{\text{hygro}}\}$ is the hygroscopic swelling strain vector, which is proportional to the coefficient of hygroscopic swelling, β_h, and the difference in local moisture content from the initial moisture content, ΔM, and is written as

$$\left\{\varepsilon^{\text{hygro}}\right\} = \Delta M[\beta_h\, \beta_h\, \beta_h\, 0\, 0\, 0]^T. \tag{14}$$

However, the moisture concentration is defined as mass concentration in the numerical model of this study, which results in the following governing equation (15) of hygroscopic swelling, representing the internal strain generated by variations in moisture content:

$$\varepsilon_{hs} = \beta_h(c_{mo} - c_{mo.ref}), \tag{15}$$

where c_{mo} is the moisture concentration at which the strain will be mobilized due to hygroscopic swelling. $c_{mo.ref}$ is the strain-free reference concentration. The hygroscopic swelling coefficient and saturated moisture concentration used in the model will be estimated values obtained through the calculation method presented by Khoshtinat et al. [37] which defines the hygroscopic swelling coefficient as a ratio of the relative linear expansion caused by moisture absorption in a dried material to the moisture concentration at saturation as defined by the following equations:

$$\beta_h = \frac{\varepsilon_{(\text{rel.moi})}}{C_{sat}}, \quad \varepsilon_{(\text{rel.moi})} = \frac{L_{sat} - L_{init}}{L_{init}}, \quad C_{sat} = \frac{M_{sat} - M_{init}}{V_{init}}, \tag{16}$$

where $\varepsilon_{(\text{rel.moi})}$ is the relevant moisture absorption-induced strain, C_{sat} is moisture concentration at saturation, and L, M, and V are the length, mass, and volume of the soil, respectively, which are evaluated from the basic experiment data carried out on Nanyang soil and listed in Table 2.

4.1.3. Coupled Subsurface Water Flow and Soil Deformation. The poroelasticity coupling in the porous media and subsurface flow module allows for the numerical coupling of Richards' equation and solid mechanics. This enables to evaluate how a soil is deformed due to fluid flow and changes in pore pressure and volume change. The interaction of fluid flow and deformation in elastic porous media is described by poroelasticity theory. The basic physics of poroelasticity in this study is driven by fluid-to-solid coupling via an initial pore fluid pressure in solid mechanics. The Navier-Stokes equation for solids is used to calculate poroelasticity.

$$-\nabla.\sigma = \rho_{av} g = (\rho_f \varepsilon_P + \rho_d) g, \tag{17}$$

where σ is the stress tensor and the body force ($\rho_{av} g$), calculated from the average density ρ_{av} of the porous medium and the gravitational acceleration g acting on it. ρ_d the density of the dry porous matrix, and ρ_f represents the fluid density.

The solid is considered to be in a quasistatic state, resulting in the disregard of inertial forces. The deformation of a poroelastic material exhibits adherence to Hooke's law of linear elasticity.

$$\sigma = C\varepsilon - \alpha_B p_f I, C = (E, \nu), \tag{18}$$

which relates the stress tensor σ with the strain tensor ε. Here, C is the drained elasticity matrix, which is represented by the Young's modulus E and the Poisson's ratio ν. The term $\alpha_B p_f$ characterizes the fluid-to-solid coupling, with α_B represent the Biot-Willis coefficient, p_f represent the pore pressure, and I which is the unity matrix. The Biot-Willis coefficient is a key poroelastic property, which relates volumetric strain to pore fluid volume (or pore pressure) and determines the degree of poroelastic response. Values of α_B range between the material porosity to 1, approaching 1 for soft media.

The linear momentum balance for a fully saturated porous solid in equilibrium under gravitational load can be written as

$$-\nabla.\sigma = -\nabla(\alpha_B p_f) + \rho_{av} g. \tag{19}$$

The fluid-to-structure coupling enters as an additional volumetric force in the momentum equation as described in Eq. (19), which describes an equilibrium state and also applies to the case of a time-dependent flow model.

The final set of coupled equations utilized in the poroelasticity multiphysics interface in COMSOL and employed in this study is presented as follows:

$$\rho_a \frac{\partial^2 u}{\partial t^2} = \nabla.(S - \alpha_B(P_A - P_{ref})I) + Fv, \tag{20}$$

$$\frac{\partial}{\partial t}(\varepsilon_p \rho_f) + \nabla(\rho_f u_f) = Q_m - \rho_f \alpha_B \frac{\partial \varepsilon_{vol}}{\partial t}, \tag{21}$$

where ε_p is the porosity, ε_{vol} is the volumetric strain, P_{ref} is the reference pressure level, and P_A is the absolute pressure.

Table 2: Parameters used in the numerical simulation.

Variable	Units	Description	Value
Nanyang soil			
g	m/s^2	Gravity	9.82
ρ	kg/m^3	Density	1550
G		Specific gravity	2.61
ϵ_p		Porosity	0.34
E	Pa	Young's modulus	$7.8e^6$
υ		Poisson's ratio	0.4
k_s	m/s	Permeability	$1.43 * 10^{-7}$
θ_s		Saturated volumetric water content	0.41
θ_r		Residual volumetric water content	0.1
H_p	m	Pressure head at upper boundary	0.15
μ_s	Pa•s	Dynamic viscosity	$8.9e^{-4}$
α_B		Biot-Willis coefficient	1
μ		Coefficient of friction	0.5
$\varepsilon_{(rel.moi)}$		Moisture absorption-induced strain	0.0214
M_{sat}	kg	Soil saturated mass	65.1
M_{dry}	kg	Soil initial mass	48.2
V_{dry}	m^3	Soil initial volume	0.0216
β_h	m^3/kg	Coefficient of hygroscopic swelling	$4e^{-5}$
D_c	m^2/s	Diffusion coefficient	$1e^{-9}$
Pile			
ρ_p	kg/m^3	Density	2700
E_p	Pa	Young's modulus	$70e^9$
υ_p		Poisson's ratio	0.3
Sand			
E	Pa	Young's modulus	$1e^6$
υ		Poisson's ratio	0.3
ρ	kg/m^3	Density	2650
k_p	m^2	Permeability	2.95e-6
ϵ_p		Porosity	0.42
α_B		Biot-Willis coefficient	1
Water			
ρ_w	kg/m^3	Density	1000
χ_f	$m•s^2/kg$	Compressibility	$4.4 * 10^{-10}$
μ	Pa•s	Dynamic viscosity	$8.9e^{-4}$

$\partial\varepsilon_{vol}/\partial t$ is the rate of change in volumetric strain of the porous matrix. The term on the right-hand side of Eq. (21) might be read as the measure of the rate at which the pore space expands. The increase in $\partial\varepsilon_{vol}/\partial t$ leads to an increase in the volume fraction that is accessible for the fluid, thus resulting in the emergence of a water infiltration, therefore the negative sign in the source term.

4.2. Geometry and Boundary Conditions. The geometry of a finite element model contends that a cylindrical concrete pile with a radius of 0.02 m and a length of 0.6 m is modelled as an isotropic elastic material placed in the center of a cylindrical domain of two soil layer specimens: Nanyang expansive soil with a radius of 0.15 m and a height of 0.5 m as the first layer and sand soil layer with a radius of 0.15 m

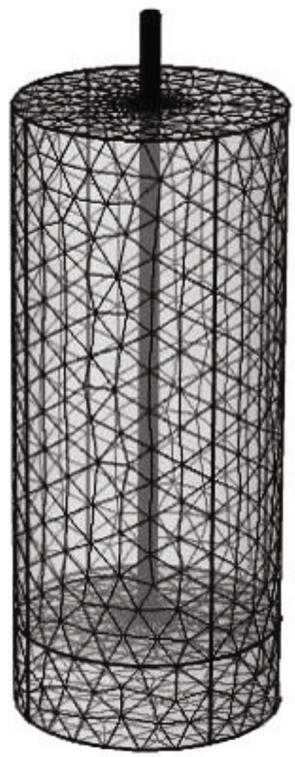

Figure 9: Geometry and meshing setup.

and a thickness of 0.1 m as the second layer, with 0.5 m of the pile length completely buried in the expansive soil layer, where this depth is considered the active zone. Following the COMSOL setup of modelling embedded structures, the geometry of the coupled interfaces was formed in the geometry sequence stage by selecting "Form an assembly" in COMSOL's model builder, which put fewer constraints on the mesh of the FE model. The mesh employed in this study is a user-controlled sequence utilizing a free triangular mesh. It consists of a total of 11,728 elements, with a degree of freedom of 67,222. The mean mesh size is determined by the maximum and minimum sizes of the mesh units for soil, which are 0.4 m and 0.072 m, respectively. The mesh located at the interface between the pile body and the surrounding soil is designed to have a finer configuration. The custom mesh technique is employed to construct the mesh of nodes at the interface between the pile and soil. The mesh units have a maximum size of 0.08 m and a minimum size of 0.008 m, as depicted in Figure 9.

The model's lateral and bottom boundary borders were constrained, while the top boundary was left unrestricted. These boundary conditions were implemented in accordance with the experimental model settings described earlier in this article. The subsurface flow module's bottom boundary is assigned an inlet flow condition from the top boundary with no flow conditions in the lateral or bottom boundaries, and the top boundary is left open for water flow. At the upper boundary, the pressure head and inlet flux were both specified and switched from one to the other during infiltration processes. First, the flow (mass flux) is determined, with the infiltration intensity assumed to be constant. Due to this difference between infiltration rate and permeability, water accumulates at the ground surface, resulting in a ponded water layer, which then requires the specification of a pressure head equal to the depth of the ponded layer. Therefore, the boundary condition that defines infiltration is changed to one that defines the pressure head that corresponds to the depth of the ponded water layer. The parameters and initial values used in the numerical model for water infiltration into unsaturated soil are presented in Table 2. The information associated with Nanyang expansive soil was obtained by experimental studies conducted on the soil, which involved evaluating its mechanical properties, soil-water retention behavior, and matching values for the coefficient of hygroscopic swelling. The parameters for pile material, sand, and water characteristics were derived from the default values specified in the material catalogue of the COMSOL software.

4.3. Simulation Result and Discussion. The surface and cross-sections of the soil-pile model in Figure 10 depict the progress of soil displacement and cumulative ground heave throughout infiltration. The side boundaries are fixed constraints in the numerical model, which is intended to limit the lateral swelling mobilization of the soil and results in an upward vertical displacement that rises with increasing infiltration time. This is noticeable in the figure, where it is possible to make out a small displacement at the side boundaries that grows vertically at greater depth and horizontally in zones close to the center of the soil domain. A 3D cut line along the soil depth and at a distance of 30 mm from the soil-pile interface was used for analyzing the result of displacement, which is shown in Figure 11. From the figure, the rise of displacement over time indicates the growth of soil ground heave at the soil surface, which was clearly identified as it increased until it reached a high value of 11.3 mm after 200 hours of infiltration. The pile displacement, on the other hand, was a reaction to the pile head load. After 50 hours of infiltration, the pile experienced a modest displacement of 1 mm. After 200 hours, the displacement peaked at 3.7 mm. This might be as a result of a decrease in matric suction, which leads to a drop in soil-pile shaft friction and a decrease in cohesiveness at the soil-pile interface following water infiltration. This may help to explain the slight increase in soil displacement that occurred at a late stage of infiltration below the pile toe. Due to the slight variations in displacement throughout the pile's length, as can be seen in Figure 11, the numerical and experimental model comparison graph depicts pile displacement as a function of infiltration time.

Although it is challenging to directly evaluate soil lateral swelling in a numerical model, a particular technique was accessible. In COMSOL, the normal stress has the opposite sign as the pressure when there is compression. In other words, positive normal stress symbolizes the effect of tension, and negative normal stress symbolizes the effect of compression. Therefore, the normal stress that the pile experiences in the active zone has been taken into account in this study. The change in normal stress levels along the soil

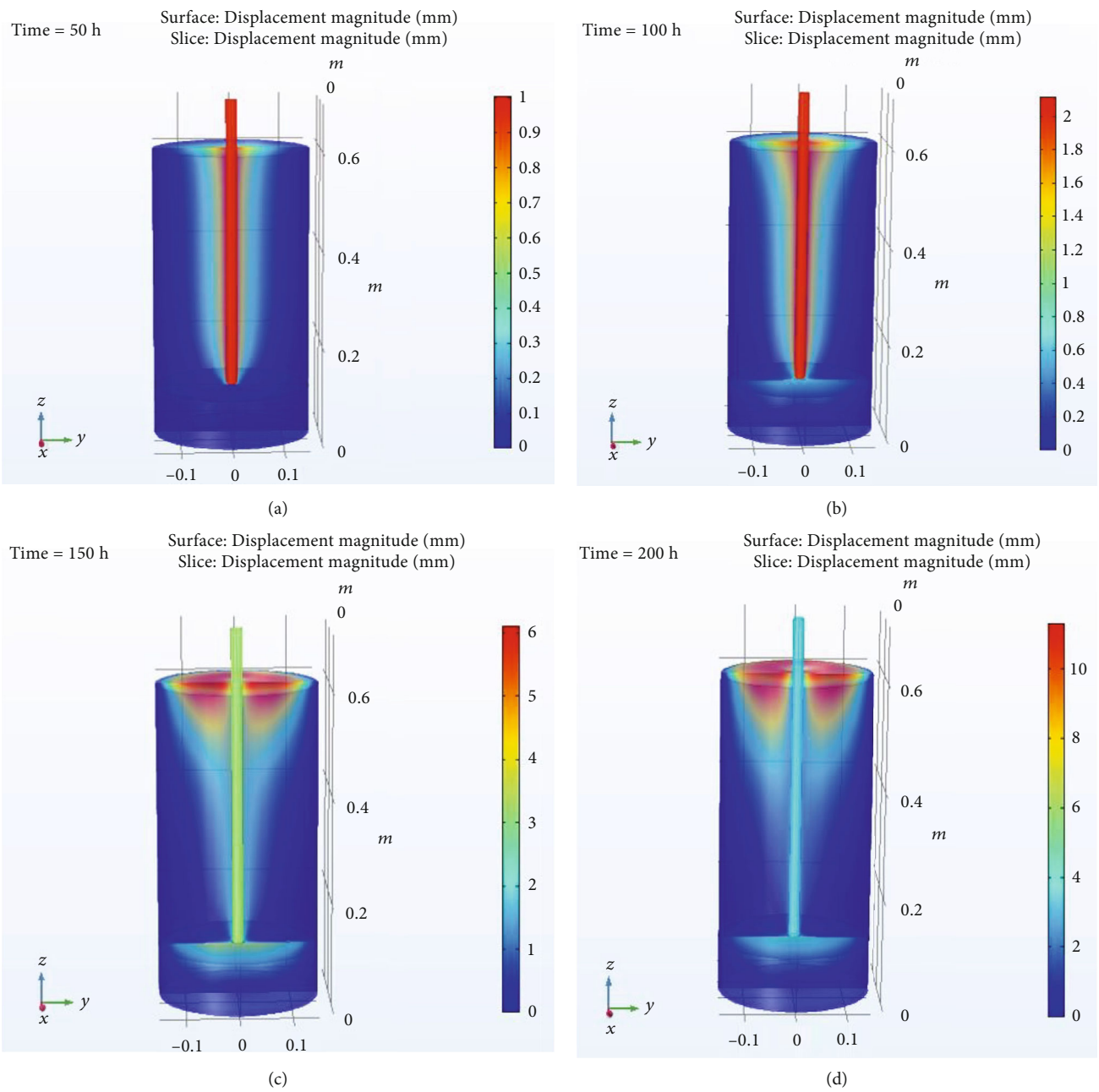

Figure 10: The variation of ground heave and pile displacement (mm) after (a) 50 h of infiltration, (b) 100 h of infiltration, (c) 150 h of infiltration, and (d) 200 h of infiltration.

active zone is shown in Figure 12 at various depths. As can be observed from the figure, normal stress rises with infiltration time while decreasing with soil depth. This phenomenon can be attributed to the early infiltration of water into the upper layers of the soil, which results in the accumulation of lateral swelling pressure that adds to the initial horizontal normal stress at the zone near the ground surface. The vertical swelling pressure that is created has a tendency to exert an upward force on the soil.

Figure 13 depicts the temporal evolution of the shear stress occurring at the interface between the soil and the pile across the length of the pile while water infiltration takes place. The supplied figure yields two discernible observations. One notable observation entails a positive correlation between the duration of infiltration and the magnitude of shear stress. The occurrence of soil ground heave and the activation of soil lateral swelling, which causes an increase in normal stress, can explain the observed behavior. The second observation concerns the apparent phenomenon that the shear stress encountered at the interface between the soil and pile attains its highest value in close proximity to the surface of the ground, gradually decreasing as the depth of the pile increases. This decrease in interface shear stress as depth increases can be attributed to the diminishing relative displacement between the soil and pile at greater depths.

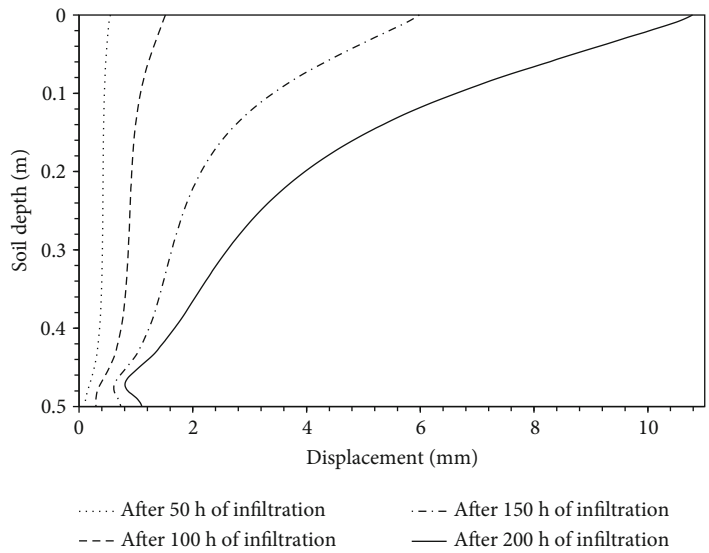

Figure 11: Displacement along the soil depth during infiltration.

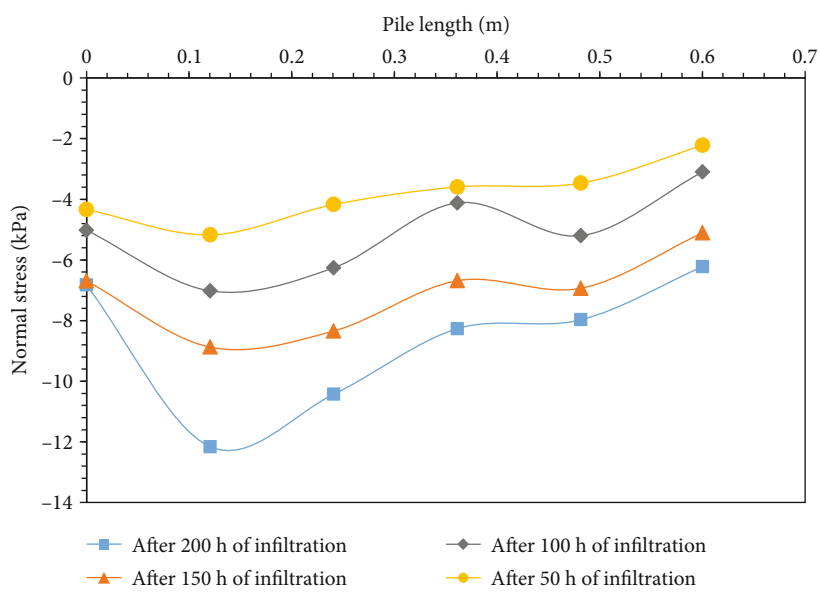

Figure 12: Variation of normal stress at soil-pile interface during infiltration.

It is vital to remember that when comparing the numerical and experimental models, simply the time when the water starts to infiltrate into the soil will be considered in the comparison graph, leaving out the experimental model's static loading phase. Figures 14 and 15 compare experimental and numerical soil ground heave and pile displacement data curves. The inclusion of estimated R-squared values for both Figures 14 and 15 is included. The R-squared values of 0.9921 and 0.9825, respectively, indicate that the experimental model's data and the numerical model's result are in good agreement.

The relationship between skin friction and the axial force of the pile when loaded indicated by Fan et al. is utilized to determine the distribution of the pile's axial force during infiltration operations. A pile's axial response is influenced by the sectional characteristics of the pile as well as the soil properties. The fluctuation of the axial force, P, down the length of the pile can be explained by [38]

$$\frac{\partial P}{\partial z} = 2\pi r_0 t_0, \tag{22}$$

where P is the pile axial force, r_0 is the radius of the pile, and t_0 is the shear stress at the pile wall.

Figure 16 shows the comparison data of the pile axial force recorded during the experiment by strain gauges and the data of the numerical model, which is calculated using Eq. (11), and as can be seen, the data of the experimental and numerical models are comparable.

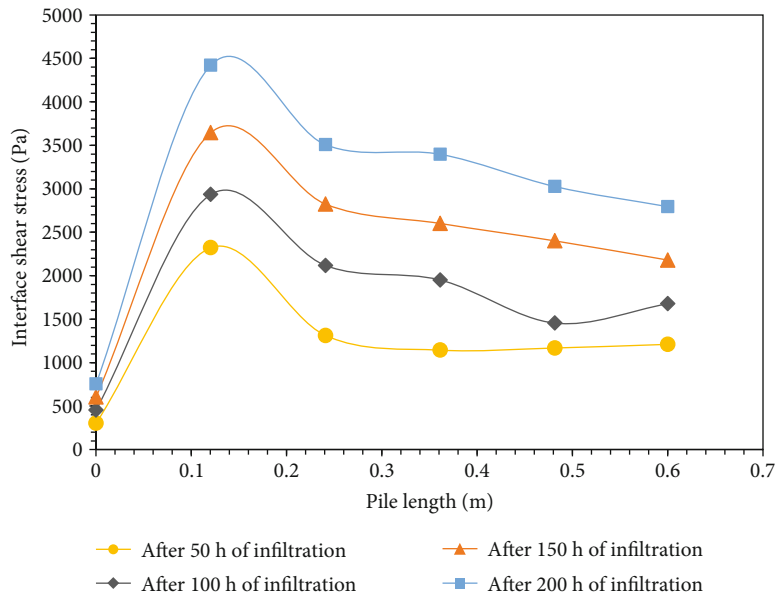

Figure 13: Shear stress distribution along the pile length during infiltration.

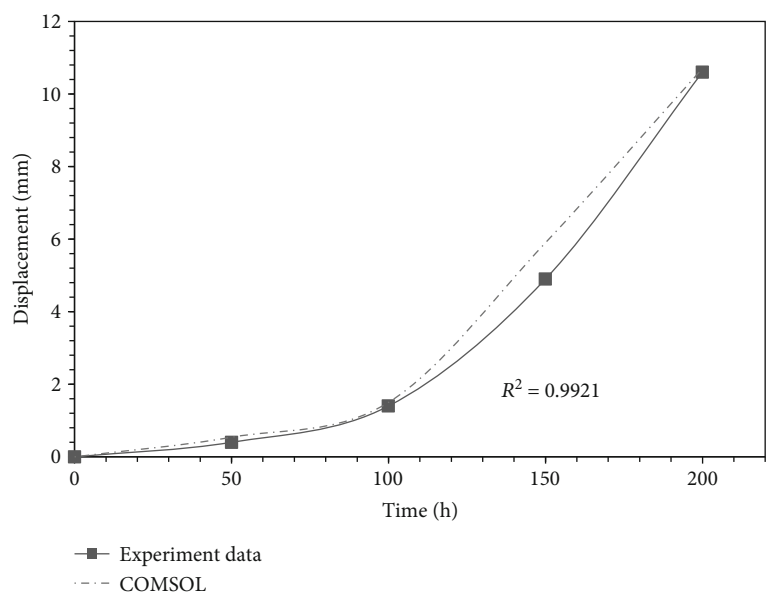

Figure 14: Soil ground heave during infiltration from experimental and numerical simulation data.

5. Conclusions

This study conducted a laboratory pile model tests under water infiltration to examine expansive soil-pile interactions during infiltration. Meanwhile the present study proposed a novel numerical simulation approach that incorporates the coupling of subsurface flow, soil deformation, and hygroscopic swelling to investigate the interaction between expansive soil and piles during water infiltration. The numerical simulation model was successfully implemented using COMSOL. The results lead to these conclusions:

(1) The lab experiment revealed that water infiltration caused ground heaves to happen, peaking at 10.7 mm after 200 hours. The pile settled 4 mm after the test with no observed upward movement. The pile base's resistivity was 22 N before infiltration. After infiltration, its resistance rose rapidly to 168 N by the test's end. This indicates that a larger amount of the pile head load gets transmitted deeper. Infiltration minimizes pile shaft friction by decreasing matric suction. Thus, the pile base supports the pile head load more

(2) The numerical model shows that hygroscopic strain of expansive soil results from water infiltration. Due to lateral soil swelling (normal stress) and ground heave, the expansive soil-pile interface shear stress gradually increases. This rise peaks at 4420 Pa

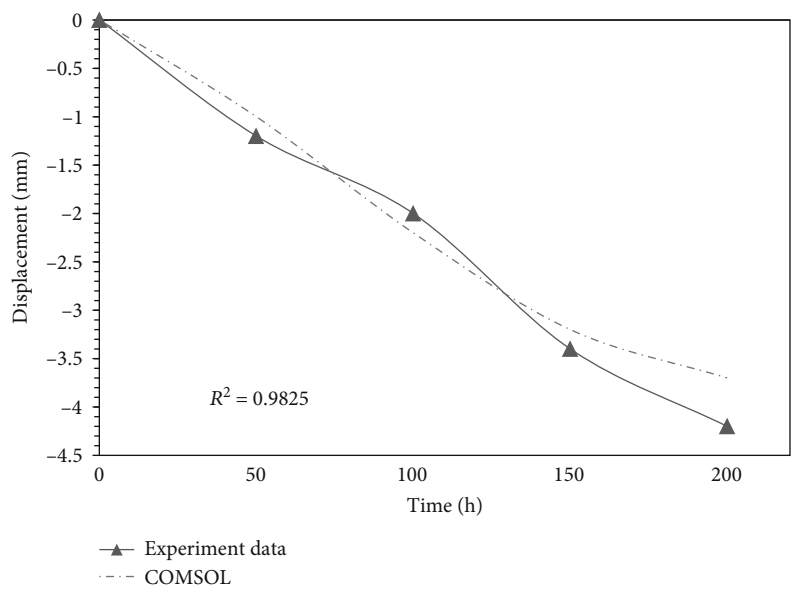

Figure 15: Experimental and numerical simulation data of pile displacement during infiltration.

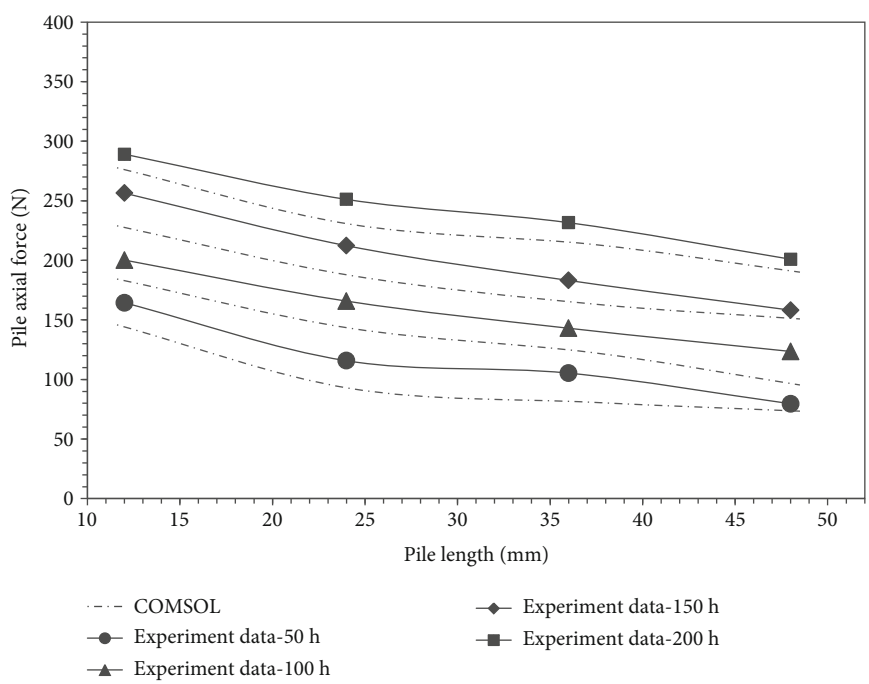

Figure 16: Experiments and numerical simulation data of pile axial force distribution upon infiltration processes.

at shallower depths, 200 hours after infiltration. Shear stress reduces with depth as expansive soil-pile relative displacement decreases

(3) The results of the numerical model have been verified through comparison with the conclusions derived from the laboratory model. The process of validation involves the comprehensive examination of both the pile and the soil displacement, together with the assessment of the axial force distribution within the pile. The level of agreement between the experimental data curve and the numerical model data curve is considered to be adequate

(4) The main focus of this study is soil-pile interactions in water infiltration. However, future studies could examine soil-pile interactions during water evaporation. In addition, factors that influenced the pile, such as the length, material, and installation method, could also be considered. Future research should evaluate the possibility of using a comprehensive-scale pile model in experimental and real-world

scenarios, taking into account diameter to D50 and pile group configuration. This investigation could be a case study to further verify the numerical technique's usefulness and correctness

Data Availability

The data used to support the findings of this study are included within the article.

Conflicts of Interest

The authors declare that there are no conflicts of interest regarding the publication of this paper.

Acknowledgments

This research was funded by the National Natural Science Foundation of China (Nos. 12172085 and 11672066).

References

[1] R. Driscoll, "The influence of vegetation on the swelling and shrinking of clay soils in Britain," *Geotechnique*, vol. 33, no. 2, pp. 93–105, 1983.

[2] C. S. Gourley, D. Newill, and H. D. Schreiner, "Expansive soils: TRL's research strategy," *Engineering Characteristics of Arid Soils*, *260*, 1993, CRC Press, p. 247, 1993.

[3] R. Schnellmann, M. Busslinger, H. R. Schneider, and H. Rahardjo, "Effect of rising water table in an unsaturated slope," *Engineering Geology*, vol. 114, no. 1-2, pp. 71–83, 2010.

[4] T.-L. Tsai and J.-K. Wang, "Examination of influences of rainfall patterns on shallow landslides due to dissipation of matric suction," *Environmental Earth Sciences*, vol. 63, no. 1, pp. 65–75, 2011.

[5] I. A. Abd, M. Y. Fattah, and H. Mekkiyah, "Relationship between the matric suction and the shear strength in unsaturated soil," *Case Studies in Construction Materials*, vol. 13, article e00441, 2020.

[6] H. Tu and S. K. Vanapalli, "Prediction of the variation of swelling pressure and one-dimensional heave of expansive soils with respect to suction using the soil-water retention curve as a tool," *Canadian Geotechnical Journal*, vol. 53, no. 8, pp. 1213–1234, 2016.

[7] Z. Dai, S. Chen, and J. Li, "Physical model test of seepage and deformation characteristics of shallow expansive soil slope," *Bulletin of Engineering Geology and the Environment*, vol. 79, no. 8, pp. 4063–4078, 2020.

[8] E. Liu, H. S. Yu, G. Deng, J. Zhang, and S. He, "Numerical analysis of seepage–deformation in unsaturated soils," *Acta Geotechnica*, vol. 9, no. 6, pp. 1045–1058, 2014.

[9] P. Pei, Y. Zhao, P. Ni, and G. Mei, "A protective measure for expansive soil slopes based on moisture content control," *Engineering Geology*, vol. 269, article 105527, 2020.

[10] J. Li, D. A. Cameron, and G. Ren, "Case study and back analysis of a residential building damaged by expansive soils," *Computers and Geotechnics*, vol. 56, pp. 89–99, 2014.

[11] A. A. B. Moghal, A. A. K. Obaid, T. O. Al-Refeai, and M. A. Al-Shamrani, "Compressibility and durability characteristics of lime treated expansive semiarid soils," *Journal of Testing and Evaluation*, vol. 43, no. 2, pp. 255–263, 2015.

[12] F. A. Yitagesu, F. van der Meer, H. van der Werff, and W. Zigterman, "Quantifying engineering parameters of expansive soils from their reflectance spectra," *Engineering Geology*, vol. 105, no. 3-4, pp. 151–160, 2009.

[13] M. Zhelnin, A. Kostina, A. Prokhorov, O. Plekhov, M. Semin, and L. Levin, "Coupled thermo-hydro-mechanical modeling of frost heave and water migration during artificial freezing of soils for mineshaft sinking," *Journal of Rock Mechanics and Geotechnical Engineering*, vol. 14, no. 2, pp. 537–559, 2022.

[14] Z. Pei-ding, S. Chao-shang, F. Xuan, L. Song-tao, W. Long-jing, and C. Zheng-zheng, "Temporal and spatial evolution mechanisms of the water-conducting fractured zone of overlying strata in the Kongzhuang coal mine," *Geofluids*, vol. 2023, Article ID 3790998, 13 pages, 2023.

[15] L. Xiao-Lei, L. Xin-Lei, W. Yue et al., "The seepage evolution mechanism of variable mass of broken rock in karst collapse column under the influence of mining stress," *Geofluids*, vol. 2023, Article ID 7256937, 10 pages, 2023.

[16] L. Wang, Z. Cao, Y. Xue et al., "Effect of weakening characteristics of mechanical properties of granite under the action of liquid nitrogen," *Frontiers in Ecology and Evolution*, vol. 11, article 1249617, 2023.

[17] T. Munaga and K. K. Gonavaram, "Influence of stratified soil system on behavior of laterally loaded pile groups: an experimental study," *International Journal of Geosynthetics and Ground Engineering*, vol. 7, no. 2, pp. 1–14, 2021.

[18] M. Y. Fattah, R. R. Al-Omari, and S. H. Fadhil, "Load sharing and behavior of single pile embedded in unsaturated swelling soil," *European Journal of Environmental and Civil Engineering*, vol. 24, no. 12, pp. 1967–1992, 2020.

[19] S. Fadhil, R. Al-Omari, and M. Y. Fattah, "Distribution of axial force and shear stress along a compression pile embedded in saturated and unsaturated swelling soil," in *Proceedings of the 20th International Conference on Soil Mechanics and Geotechnical Engineering*, pp. 3271–3276, Rahman and Jaksa, 2022.

[20] T. Munaga, M. M. Khan, and K. K. Gonavaram, "Axial and lateral loading behaviour of pervious concrete pile," *Indian Geotechnical Journal*, vol. 50, no. 3, pp. 505–513, 2020.

[21] Y. Liu and S. K. Vanapalli, "Mechanical behavior of a floating model pile in unsaturated expansive soil associated with water infiltration: laboratory investigations and numerical simulations," *Soils and Foundations*, vol. 61, no. 4, pp. 929–943, 2021.

[22] I. A. Ruwaih, "Experiences with expansive soils in Saudi Arabia," in *Proceedings of the 6th international conference on expansive soils*, pp. 317–322, New Delhi, India, 1987.

[23] J. Nelson and D. J. Miller, *Expansive Soils: Problems and Practice in Foundation and Pavement Engineering*, John Wiley & Sons, New York, 1997.

[24] K. W. Hou, J. Jiang, S. W. Wang, and X. D. Ou, "Physical model test and theoretical study on the bearing behavior of pile in expansive soil subjected to water infiltration," *International Journal of Geomechanics*, vol. 21, no. 6, article 06021014, 2021.

[25] S. Y. Kwon and M. Yoo, "Study on the dynamic soil-pile-structure interactive behavior in liquefiable sand by 3D numerical simulation," *Applied Sciences*, vol. 10, no. 8, p. 2723, 2020.

[26] L. Qu, X. Ding, G. Kouroussis, and C. Zheng, "Dynamic interaction of soil and end-bearing piles in sloping ground: numerical simulation and analytical solution," *Computers and Geotechnics*, vol. 134, article 103917, 2021.

[27] N. X. Tran, K. Y. Gu, M. Yoo, and S. R. Kim, "Numerical evaluation of slope effect on soil–pile interaction in seismic analysis," *Applied Ocean research*, vol. 126, article 103291, 2022.

[28] M. T. Van Genuchten, "A closed-form equation for predicting the hydraulic conductivity of unsaturated soils," *Soil Science Society of America Journal*, vol. 44, no. 5, pp. 892–898, 1980.

[29] J. D. Nelson, E. G. Thompson, R. W. Schaut, K. C. Chao, D. D. Overton, and J. S. Dunham-Friel, "Design procedure and considerations for piers in expansive soils," *Journal of Geotechnical and Geoenvironmental Engineering*, vol. 138, no. 8, pp. 945–956, 2012.

[30] Y. Liu and S. K. Vanapalli, "Load displacement analysis of a single pile in an unsaturated expansive soil," *Computers and Geotechnics*, vol. 106, pp. 83–98, 2019.

[31] Z. Zhong-miao, Z. Qian-qing, and Y. Feng, "A destructive field study on the behavior of piles under tension and compression," *Journal of Zhejiang University-Science A*, vol. 12, no. 4, pp. 291–300, 2011.

[32] E. H. Wong, R. Rajoo, S. W. Koh, and T. B. Lim, "The mechanics and impact of hygroscopic swelling of polymeric materials in electronic packaging," *Journal of Electronic Packaging*, vol. 124, no. 2, pp. 122–126, 2002.

[33] M. H. Shirangi and B. Michel, "Mechanism of moisture diffusion, hygroscopic swelling, and adhesion degradation in epoxy molding compounds," in *Moisture Sensitivity of Plastic Packages of IC Devices. Micro- and Opto-Electronic Materials, Structures, and Systems*, X. Fan and E. Suhir, Eds., pp. 29–69, Springer, Boston, MA, USA, 2010.

[34] Y. He, "Moisture absorption and hygroscopic swelling behavior of an underfill material," *Thermochimica Acta*, vol. 546, pp. 143–152, 2012.

[35] J. Chang, J. Xiao, J. Q. Jiang et al., "Study on hygroscopic swelling and dehumidification cracking characteristics of expansive soil under acid rain and cyclic drying-wetting," *Advances in Civil Engineering*, vol. 2021, Article ID 8834583, 10 pages, 2021.

[36] J. H. Perez, F. Tanaka, and T. Uchino, "Comparative 3D simulation on water absorption and hygroscopic swelling in japonica rice grains under various isothermal soaking conditions," *Food Research International*, vol. 44, no. 9, pp. 2615–2623, 2011.

[37] S. Khoshtinat, V. Carvelli, and C. Marano, "Characterization and modeling the hygroscopic behavior of cellulose acetate membranes," *Cellulose*, vol. 29, no. 4, pp. 2175–2186, 2022.

[38] Z. H. Fan, Y. H. Wang, H. B. Xiao, and C. S. Zhang, "Analytical method of load-transfer of single pile under expansive soil swelling," *Journal of Central South University of Technology*, vol. 14, no. 4, pp. 575–579, 2007.